# Multi-angle color prediction of glossy anodized titanium samples through the determination of the oxide layer structural parameters

M. Maillet, Quentin Cridling, M. Lenci, Mariapia Pedeferri, Charrière Renée

# Multi-angle color prediction of glossy anodized titanium samples through the determination of the oxide layer structural parameters

**Maxence Maillet,[1,3] Quentin Cridling,[1,2] Matthieu Lenci,[1] MariaPia Pedeferri,[2] and Renee Charriere,[1,*]**

[1]*Mines Saint-Etienne, Univ Lyon, CNRS, UMR 5307 LGF, Centre SMS, F - 42023 Saint-Etienne France*
[2]*Politecnico di Milano, Department of Chemistry, Materials and Chemical Engineering Giulio Natta, Milan, Italy*
[3]*Currently with the Université de technologie de Compiègne, CNRS, Biomechanics and Bioengineering, Centre de recherche Royallieu - CS 60319 - 60203 Compiègne Cedex, France*
**Corresponding author: renee.charriere@emse.fr*

Received XX Month XXXX; revised XX Month, XXXX; accepted XX Month XXXX; posted XX Month XXXX (Doc. ID XXXXX); published XX Month XXXX

**The purpose of the present study is to predict the whole chromatic path travelled by the colors of glossy anodized titanium samples in every specular geometry. It is based on measurements of the samples reflectance spectra in a limited number of specular geometries which allow to obtain the oxide layer structural parameters (thickness, refractive index) which are then put into an optical model to predict the samples reflectance spectra in every specular geometry. A good color prediction performance is obtained, with an average $\Delta E_{94}$ color distance over all samples and geometries of 1.9. The oxide layer structural parameters are also in good agreement with refractive index values extracted from the literature and thicknesses measured on electron microscopy images of samples sections.** 

Doi....

## 1. INTRODUCTION

Being able to characterize properly the color of gonioapparent materials (i.e. materials which colors depend on the illumination and/or observation directions) remains a challenge. Entirely characterizing the material color appearance would require to measure its color for each illumination and observation direction in the hemisphere above the sample. As this process would be extremely time consuming, the development of models predicting the material color for any illumination/observation geometry based on color measurements in a limited number of geometries is an active research field.

Color predictions of various gonioapparent materials can be found in the literature. Special-effect coatings, which are composed of interferential flakes embedded in a transparent colored substrate, are highly gonioapparent and well-known in the car paint industry. Nadal et al. [1] showed that 15 different geometries are necessary for the colorimetric characterization of such samples. All these geometries are in the incidence plane, and composed of 3 different incidence angles (15°, 45° and 65°) and a set of 5 different non-specular observation angles for each incidence angle. The authors implemented fourth-order polynomial fits of the CIELAB [2] color components of a sample composed of a red-blue pearlescent coat with a bright red base. The fits were performed for each incidence angle using the 5 selected observation angles. The authors then compared the color components obtained from the fit with the color components obtained from 30 in-plane Bidirectional Reflectance Distribution Function (BRDF) measurements (2 incidence angles of 15° and 65° and 15 observation angles for each) using the $\Delta E\ CMC(2:1)$ [3] color distance : an average value of 0.3 and a maximum value of 1.5 are obtained. Ferrero et al. [4] predicted the whole spectral BRDF of special-effect coatings from reflectance measurements in only 9 geometries. These geometries are all included in the incidence plane and correspond to two different incidence angles (20° and 50°) and 7 different observation angles. The authors used a principal components analysis to extract the key features of the BRDF and extract the minimum number of geometries necessary to predict the whole BRDF. They then checked the color prediction performance on 448 BRDF measurements for two samples called Arctic Fire and Lapis Sunlight. Average and maximum $\Delta E_{ab}$ [2] color distance values are respectively 7 and 42 for the first sample, and 6.5 and 36 for the second one. Further work of Ferrero et al. [5] on 15 samples of special effect coatings compared the color prediction performance

obtained with the nine previous geometries and with geometries of commercial multi-angle spectrophotometers. The authors obtained comparable results with average $\Delta E_{ab}$ values over all samples (checked on the same previous 448 BRDF measurements) between 5 and 5.5 with two commercial spectrophotometers. The first spectrophotometer has 15 measurement geometries corresponding to two incidence angles (45° and 15°) and 8 different observation directions. Four of these geometries are outside of the incidence plane. The second spectrophotometer has 10 in-plane geometries corresponding to 3 different incidence angles and 8 different observation directions.

Periodically structured materials are also often gonioapparent materials. Højlund-Nielsen et al. [6] characterized and modelled the specular colors of silicon diffraction gratings with a square lattice. Such gratings exhibit also highly anisotropic colors. The authors modelled the sample colors through Rigorous Coupled-Wave Analysis simulations. This is an electromagnetic model taking into account the material structure and refractive indexes. They obtained a very good visual agreement between simulated and measured colors for incidence angles from 0° to 70° and for two different orientations of the samples. Unfortunately, the authors didn't estimate the color prediction performance in terms of standard color distances.

Note that other models can be found in the literature to predict the colors of materials (not necessarily gonioapparent ones). For example Kim et al. [7] computed the colors of TiN and ZrN for various electron doping levels using a full ab initio procedure determining the dielectric function of the material. Baxter et al. [8] used a deep-learning process to predict plasmonic colors generated by picosecond laser coloring of silver.

Anodized metals can also be gonioapparent, and it is the case in particular for anodized titanium due to the interferential origin of its colors [9]. Despite the colors of anodized titanium are well-known and characterized [10–16], their gonioapparent features aren't well studied. Indeed, the anodized titanium colors are usually characterized through commercial spectrophotometers with standard 45°/0° or 8°/diffuse fixed geometries which don't allow to measure the gonioapparent behavior of the material. More generally, the gonioapparent colors of anodized metals are neither well characterized nor modelled. Komatsu et al. [17] characterized the specular reflectance and colors of anodized niobium samples for Transverse Electric (TE) and Transverse Magnetic (TM) polarized light for incidence angles from 5° to 70°, but didn't propose a model to predict these colors. Manzano et al. [18] developed an empirical model to predict the CIE 1931 xy chromaticity coordinates of nanostructured anodized aluminum samples covered with a metal layer as a function of the oxide layer thickness. Nevertheless, this empirical model isn't based on an optical model of the material, and no study of the color variations with the incidence and/or the observation angle is presented.

The purpose of the present study is to predict the whole chromatic path travelled by the colors of glossy anodized titanium samples in every specular geometry. The study is based on measurements of the samples reflectance spectra in a limited number of specular geometries. It allows to obtain the oxide layer structural parameters (thickness, refractive index) which are then put into an Abeles matrices [19] based optical model to predict the samples reflectance spectra in every specular geometry. The coherence of the obtained oxide layer structural parameters is checked by comparisons with either extracted values from the literature or Scanning Transmission Electron Microscope (STEM) images of Focused Ion Beam (FIB) lamellae of certain samples. The method presented in this paper can be extended to any gonioapparent sample which reflectance can be correctly modeled through a multilayer Abeles matrices model.

## 2. MATERIALS AND METHODS

### A. Description of the samples

Six samples were cut out from a 1 mm thick ASTM Grade 2 titanium sheet. A simple polishing with a SiC P300 grinding paper was first performed. Then, a complete mechanical polishing has been carried out, including diamond paste solutions from 6 µm to 1 µm and a final step using a grinding cloth and an alumina solution with a particle size of 0.6 µm. Two different series of three samples were prepared with two different roughness levels. The first series referred to as "Alumina" or "Alu" isn't further polished. The second series referred to as "Vibromet" or "Vib" is then submitted to a vibratory polisher, Buehler Vibromet2, with a 60 mm colloidal solution. All samples were polished separately, one by one. The typical roughness of the "Alumina" and "Vibromet" series samples corresponds respectively to $S_a$ roughness parameters [20] of about 60 nm and 15 nm. More details about the samples roughness can be found in the supplemental document.

The samples were anodized in a galvanostatic regime by imposing a current density equal to 20 mA/cm$^2$. The counter electrode is circular and made of activated titanium. All experiments were performed in a 0.5 M sulfuric acid electrolytic solution ($H_2SO_4$) at room temperature. The cell potential increases gradually during the anodizing process. When the potential reaches a desired value, the current is shut down and the sample is removed from the bath. Three different maximum cell potentials values have been chosen: 10 V, 20 V and 90 V, corresponding respectively to 3 s, 5 s and 100 s anodizing times.

Fig. 1 is a picture of the six samples prepared in the present study. The samples exhibit different interferential colors due to different oxide thicknesses.

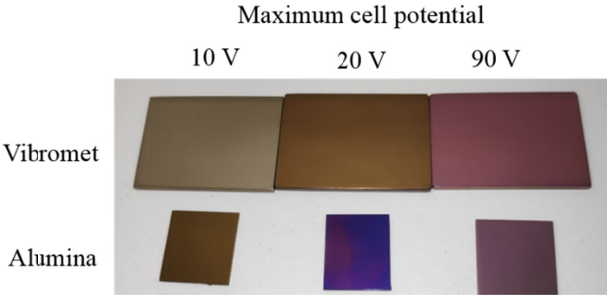


Fig. 1. Picture of the six samples considered in the present study with the value of the maximum cell potential for each sample. The picture has been taken under diffuse daylight, with a camera having an automatic white balance.

### B. Electronic images of samples cross-sections

The oxide layer of the Vibromet series samples anodized at maximum cell potentials of 20 V and 90 V have been characterized by STEM imaging of FIB cut lamellae of these samples. FIB cutting

of sample cross-sections has been preferred over other techniques, as for example putting a slice of the sample in a resin, because the polishing process needed in this case could spread the oxide layer and modify its thickness. The lamellas preparations were achieved in a FEI Helios 600i dualbeam (focused Gallium (Ga) ions beam and Field Emission Gun-Scanning Electron Microscopy electrons column) workstation. First, a Platinum (Pt) protective layer was deposited on the sample surface. Then, few microns deep cross sections were milled on both sides of the Pt deposit. The lamellas were lift out and slid on a copper grid. The lamellas were thinned with the Ga ion beam until a thickness of about 100 nm. A low kV (5 kV) cleaning was finally applied on both sides of the lamellas, in order to remove most of the surface layer damaged by the ion beam. The length of the thin part of the lamellas was of a few microns. Thereafter, inside the dualbeam, images were acquired in the thin part of the lamella, along the oxide layer, the lamella plane being parallel to the STEM detector plane. The STEM detector is made of several concentric parts. The images were acquired with the intermediate part of the annular detector. The acceleration voltage was 30 kV.

### C. Optical measurement protocol

Reflectance measurements were carried out with an in-plane goniometer (see Fig. 2) in the wavelength range [370 nm – 800 nm]. Samples were illuminated with a broadband laser-driven white light source (ENERGETICS LDLS EQ-99XFC) linked to the goniometer through a 100 µm diameter core optical fiber (BBFIBERX-100-2M-FC-015-REV2). Light was collimated with a 50 mm focal lens (THORLABS AC254-050-A-ML). The central part of the beam was selected through a 10 x 2 mm rectangular hole in order to maximize the illuminated area on the sample while maintaining a beam size smaller than the sample at grazing incidence angles. The light reflected by the sample was collected with a 5.08 cm diameter 4-port integrating sphere (Newport 819C-SL-2) placed about 7 cm far from the rotation axis of the goniometer. The entrance port of the sphere has a diameter of 12.7 mm. The integrating sphere is connected to a UV-visible spectrometer (Avantes SensLine AvaSpec-ULS2048XL-EVO) through a 1 mm core diameter quartz optical fiber (LOT UV1000 B 932). Reflectance was measured with non-polarized (NP), TE and TM polarized light. Light was polarized with a polarizer (Edmund Optics #54926) placed between the hole and the sample on the goniometer arm.

Before measurement, alignment of the beam was checked, and the orientation of the sample was adjusted by overlaying the hole with the light reflected by the sample at normal incidence. Reflectance spectra were measured in specular geometry (incidence angle $\theta_i$ and observation angle $\theta_r$ equal to each other) at 9 angles: 75°, 70° ,65°, 60°, 45°, 40°, 30°, 20° and 15°. The experimental reflectance value $R^P_{expe}$ for polarization $P = NP$, $TE$ or $TM$ is obtained through the following formula:

$$R^P_{expe} = \frac{S^P_{sample} - S_{dark}}{S^P_{direct} - S_{dark}}, \quad (1)$$

where $S^P_{sample}$, $S^P_{direct}$ and $S_{dark}$ are the signals measured on the spectrometer respectively for $P$ polarized light when light is reflected on the sample, when the source and detection arms are aligned to each other ($\theta_i = \theta_r = 90°$ in Fig. 2 with sample holder removed) and when the light source is blocked by a black cover.

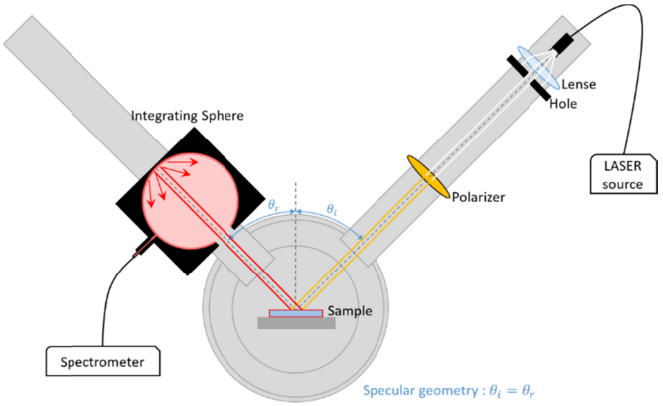


Fig. 2. Goniometer and optical setup. The reflectance measurements are carried out in the specular geometry $\theta_i = \theta_r$.

### D. Optical model

A three-layer model was proposed to describe the titanium oxide layer (Fig. 3). The oxide layer is split into three layers: an external one (identified with number 3) whose thickness is noted as $L_3$ and is composed for half of air and for half of $TiO_2$, an intermediate layer (identified with number 2) whose thickness is noted as $L_2$ and is composed of $X$% of air and $(1 - X)$% of $TiO_2$ with $X$ called the porosity of the layer, and an internal layer (identified with number 1) whose thickness is noted as $L_1$ and is composed for half of Ti and for half of $TiO_2$. This three-layer model has been preferred over two-layer or one-layer models based on STEM images of FIB cut lamellae of the Vibromet 20V and 90 V samples (see Fig. 14). A three-layer structure of the oxide layer has also been observed by L. Bartlett in [21] for anodized titanium samples. The 50/50 mix for the 1st and 3rd layers has been chosen arbitrarily, by analogy to what is traditionally done in ellipsometric models for intermediate roughness layers [22]. In this model, Cauchy's equation is used for the calculation of the $TiO_2$ refractive index $n_{TiO_2}(\lambda)$ at the wavelength $\lambda$:

$$n(\lambda) = A + \frac{B}{\lambda^2}, \quad (2)$$

with $A$ and $B$ two coefficients that will be determined by a fit of the samples reflectance spectra.

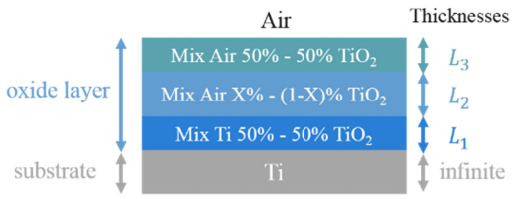


Fig. 3. Anodized titanium sample model used for the simulated spectra.

Titanium refractive index is extracted from [23] (see Fig. S1 for the values). Titanium refractive index is extracted from the literature, contrary to $TiO_2$ due to the different crystalline phases of $TiO_2$ with different refractive indexes which can be present in anodized $TiO_2$ [24]. Bruggeman effective medium theory ([25] and supplemental document) is used to compute the average refractive

index of the layers composed of a mix of two different materials. Simulated reflectance spectra are computed through an Abeles matrices based model [19] using the 6 parameters : $L_1, L_2, L_3, X, A$ and $B$ described above. These six parameters are obtained for each sample by fitting experimental reflectance spectra both for TE and TM polarized incident light for different sets of incidence angles. The fit procedure uses a chi-square ($\chi^2$) minimization. The $\chi^2$ parameter is computed the following way:

$$\chi^2 = \frac{\sum_{\theta_i}\sum_{\lambda}\left(R^{TE}_{expe}(\lambda,\theta_i) - R^{TE}_{simu}(\lambda,\theta_i)\right)^2}{\sum_{\theta_i} 1} + \frac{\sum_{\theta_i}\sum_{\lambda}\left(R^{TM}_{expe}(\lambda,\theta_i) - R^{TM}_{simu}(\lambda,\theta_i)\right)^2}{\sum_{\theta_i} 1} \quad (3)$$

where $\lambda$ is the wavelength, $\theta_i$ the incidence angle, $R^{TE}_{expe}$ (resp. $R^{TM}_{expe}$) the experimental reflectance spectrum for TE (resp. TM) polarized incident light, $R^{TE}_{simu}$ (resp. $R^{TM}_{simu}$) the simulated reflectance spectrum for TE (resp. TM) polarized incident light. $\sum_{\theta_i} 1$ will be equal to the number of incidence angles chosen to fit the material parameters. To avoid issues linked to initial parameters in minimization problems, 100 $\chi^2$ minimizations were made with random initial parameters uniformly chosen in the ranges presented in Table S2Table . These ranges correspond to wide ranges of possible values for the different parameters. They have been checked a posteriori by looking at the final parameter values obtained after the fitting process.

The process gives thus 100 sextuplets of result parameters. Among these sextuplets, these with a $\chi^2$ superior to 6 times the median $\chi^2$ and these with $X$>0.5 were removed. Fig. S2 illustrates two examples of the effect of these first selection steps on the selected $\chi^2$ values. This value of 0.5 has been chosen arbitrarily. It is indeed difficult in the present model to have a precise estimation of the porosity of the layer as the same refractive index for the layer number 2 can be obtained for different sets of the parameters $\{A, B, X\}$. It thus implies that two samples with similar $X$ values do note necessarily have the same porosity for layer 2, as the $A$ and $B$ parameters might already include a fraction of the porosity. Then, the most probable sextuplets were selected with the following process (see Fig. 4): for each sample, a Gaussian fit was applied to the repartition of the thickness values of each layer. Let's denote respectively by $\mu_i$ and $\sigma_i$ ($i \in [\![1,3]\!]$) the average and standard deviation of the thickness values of the layer number $i$. The intervals $[\mu_i - \sigma_i, \mu_i + \sigma_i]$ are represented as green lines in Fig. 4 at an amplitude equal to the Gaussian fit maximum divided by $\sqrt{2}$. Only the parameter sextuplets that fulfill the following condition were selected: $L_1^j \in [\mu_1 - \sigma_1, \mu_1 + \sigma_1] \cap L_2^j \in [\mu_2 - \sigma_2, \mu_2 + \sigma_2] \cap L_3^j \in [\mu_3 - \sigma_3, \mu_3 + \sigma_3]$,where $L_i^j$ is the thickness of the layer $i$ of the parameter sextuplet number $j$ (with $j \in [\![1,100]\!]$). Then, after this selection process, the sextuplet with the lowest $\chi^2$ value is extracted and will give the retained values for the 6 parameters $L_1, L_2, L_3, X, A$ and $B$. The purpose of this selection process is to obtain the best compromise between the $\chi^2$ value and the reliability of the 6 material parameters. Examples of fit results for high $\chi^2$ values and for low $\chi^2$ values in cases where the material parameters are selected or not are presented in Fig S3 and Table S3.

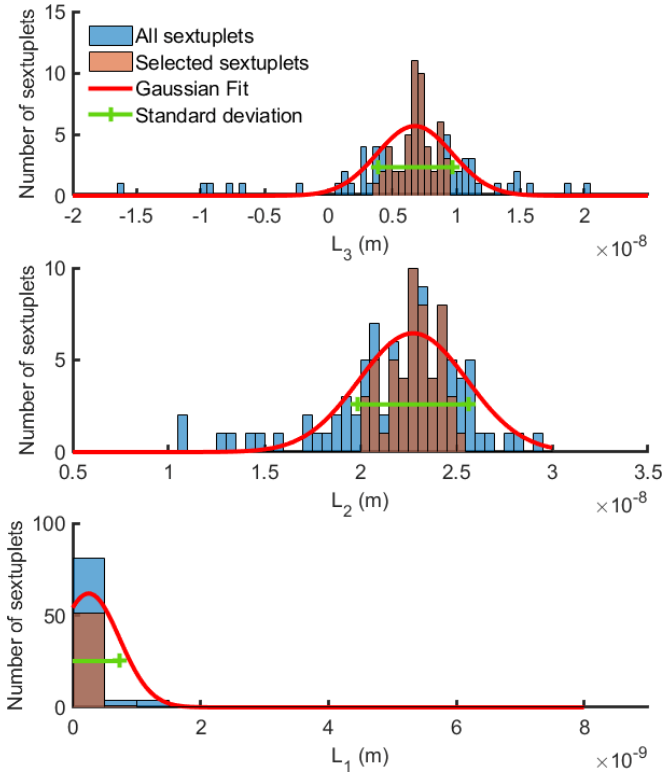


Fig. 4. Example of selection process of the sextuplets according to the layers thicknesses values. Each histogram bin has a width of 0.5 nm. This example corresponds to the Vib 20 V sample with a fit of the material parameter done on three incidence angles (65°, 70° and 75°).

## 3. RESULTS

### A. Reflectance and color prediction

Once the material parameters obtained thanks to the process described in the previous section, the samples reflectance spectra are computed for all 9 incidence angles. The material parameters fit process has been done with different sets of incidence angles: $\{15°\}$, $\{45°\}$, $\{75°\}$, $\{15°, 45°\}$, $\{15°, 75°\}$, $\{45°, 75°\}$, $\{15°, 45°, 75°\}$, $\{20°, 40°, 70°\}$, $\{65°, 70°, 75°\}$, $\{15°, 20°, 30°\}$ and $\{15°, 30°, 45°, 60°, 75°\}$. An example of the process flow from the reflectance measurements to the color prediction is presented in Fig. 5 in the case where the fit process is done on the angle set $\{45°, 75°\}$. To evaluate the performance of the prediction of the samples colors, the experimental and simulated spectra have been converted to CIELAB color coordinates ([2] and supplemental document) assuming a D65 illuminant. Then the difference between the simulated and experimental colors have been evaluated through the $\Delta E_{94}$ metric ([2] and supplemental document). The $\Delta E_{94}$ metric has been preferred over the most recent CIEDE2000 metric as it is more widely used in the literature. It thus facilitates the comparison between the color prediction performances presented in the present paper and other publications. Fig. 6 represents the average and maximum $\Delta E_{94}$ values over all samples and incidence angles as a function of the set of incidence angles used to fit the material parameters.

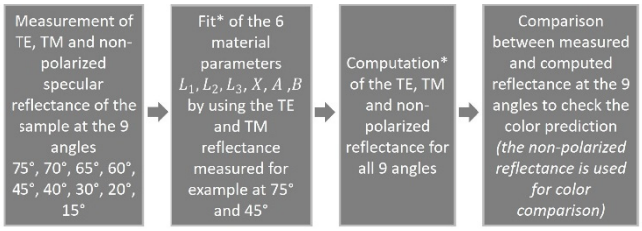


Fig. 5 : Example of the color prediction process flow in the case where the color prediction is made on the set of angles {45°,75°} for one sample.

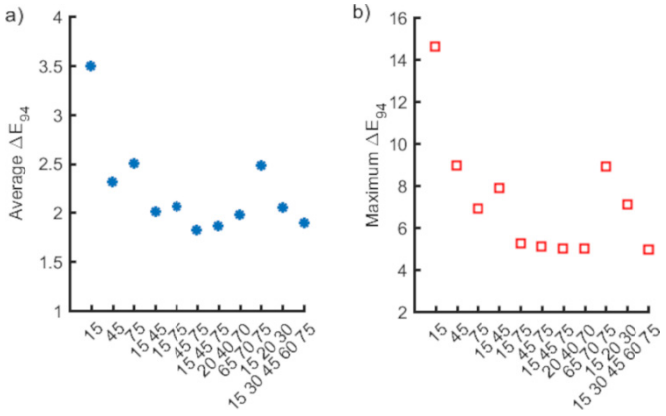


Fig. 6 : (a) Average and (b) maximum $\Delta E_{94}$ values over all samples and incidence angles as a function of the set of incidence angles used to fit the material parameters.

Higher values of both the average and maximum $\Delta E_{94}$ are observed when the material parameters are fit on only one incidence angle. In the case of two or three incidence angles, the performance of the color prediction depends on the angles chosen for the fit. The lowest values for both the average and maximum $\Delta E_{94}$ are obtained for the angle sets $\{45°, 75°\}$ and $\{15°, 45°, 75°\}$. These values are comparable with the case of five incidence angles. The color prediction performance thus depends on how the incidence angles chosen for the fit are spread over [0°, 90°]. To illustrate more in details the influence of the set of incidence angles on the color prediction performance, five different sets of incidence angles have been selected: the four sets of 3 incidence angles and the set of 5 incidence angles. For the sake of clarity, it what chosen not to present all angles sets, and these particular ones illustrate well the angular behavior of the $\Delta E_{94}$ values. Fig. 7 presents for all samples the $\Delta E_{94}$ values between experimental and simulated colors for all incidence angles and these five different sets of incidence angles.

The first thing that is observed in Fig. 7 is that three sets of incidence angles give almost the same results: determining the material parameters either on the sets of incidence angles $\{15°, 45°, 75°\}$, $\{20°, 40°, 70°\}$ or $\{15°, 30°, 45°, 60°, 75°\}$ doesn't change a lot the performance of the color prediction. Thus, fitting the material parameters on 5 angles instead of 3 doesn't improve the color prediction. For the two other sets, $\{65°, 70°, 75°\}$ and $\{15°, 20°, 30°\}$ , which correspond respectively to the three highest and three lowest angles, the $\Delta E_{94}$ values aren't well balanced over all incidence angles. The $\Delta E_{94}$ values are lower for the angles used to compute the material parameters, but a worsening of the color prediction performance is observed for the other angles. A better overall color prediction performance is thus obtained when the set of angles used to compute the material parameters is well distributed within the [0°, 90°] interval.

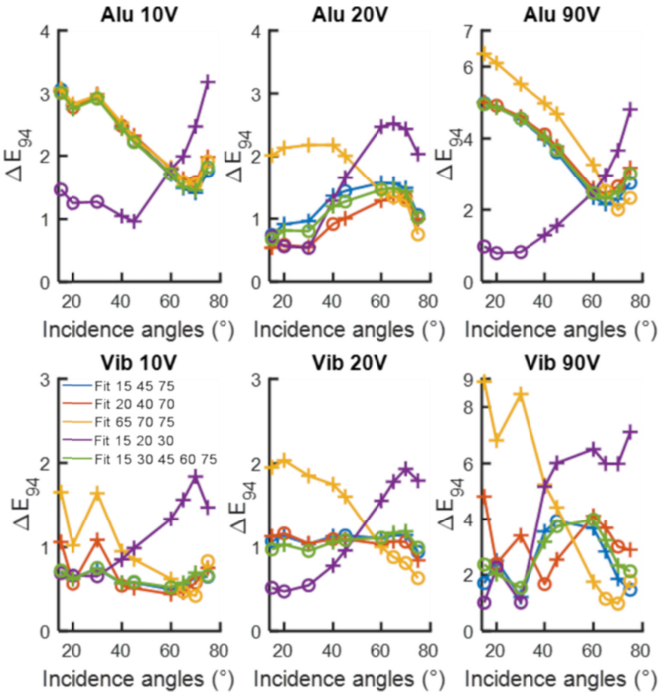


Fig. 7 : $\Delta E_{94}$ between experimental and simulated reflectance spectra for all samples as a function of the incidence angle for the 5 different sets of incidence angles used to compute the material parameters. The ∘ markers indicate angles used to fit the material parameters and the + markers indicate the other angles.

From now on, we will focus on the results obtained with the set of angles $\{15°, 45°, 75°\}$ which gives a well-balanced color prediction over all angles as well as one of the three best color prediction performances in terms of average and maximum $\Delta E_{94}$ values over all samples and angles (see Fig. 6).

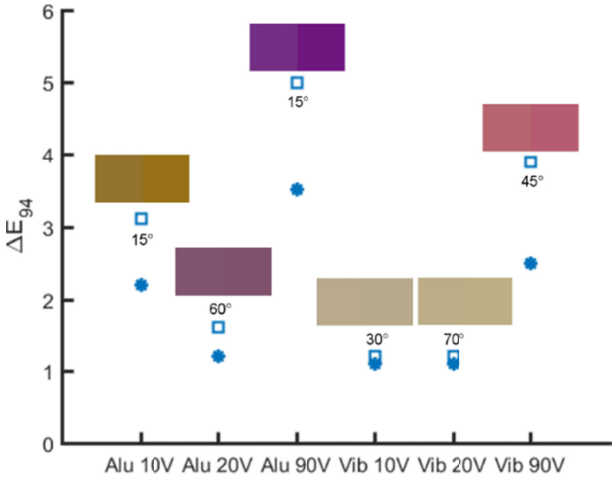


Fig. 8: Maximum □ and average ✷ $\Delta E_{94}$ values over all angles for all samples in the case where the material parameters are fit on the set of incidence angles {15°, 45°, 75°}. The angles where the maximum $\Delta E_{94}$ values occur are also indicated in the graph. The colored areas correspond to comparisons between experimental colors (left part of the area) and simulated colors (right part of the area) corresponding to the maximum $\Delta E_{94}$ values.

Fig. 8 presents the maximum and average $\Delta E_{94}$ values over all angles for all samples in the case where the material parameters are fit on the set of incidence angles {15°, 45°, 75°}. For all samples, the average $\Delta E_{94}$ is below 3.5 and the maximum $\Delta E_{94}$ is below 5, with highest average and maximum values both obtained for the Alu 90V sample. To give an idea about the performance of the color prediction, the experimental and simulated spectra in the worst cases (maximum $\Delta E_{94}$ values) have been converted to sRGB ( [26] and supplemental document) colors and displayed side by side in the graph. The color difference is perceptible for the Alu 10V, Alu 90V and Vib 90V samples, but hardly distinguishable for the other ones.

The good color prediction is associated with a good prediction of the samples spectral reflectance. Fig. 9 presents the experimental and simulated spectral reflectance for TE, TM and non-polarized incident light for the Vib 20V sample at an incidence angle of 70° and the Alu 90V sample at an incidence angle of 15°, corresponding respectively to the lowest and highest values of the maximum $\Delta E_{94}$. Note that 15° corresponds to an angle used to compute the material parameters where 70° doesn't.

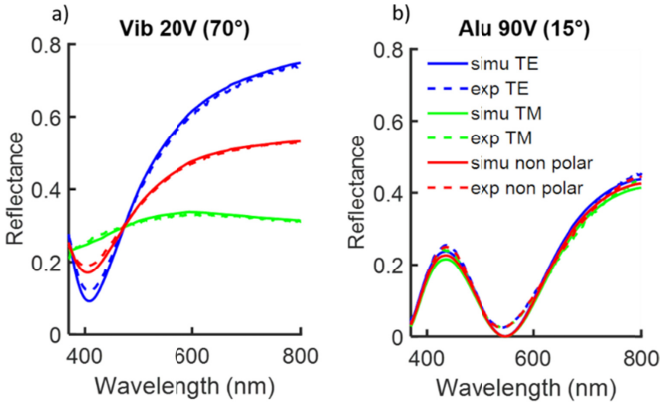


Fig. 9: Simulated (solid lines) and experimental (dashed lines) reflectance spectra for TE (blue lines), TM (red lines) and non-polarized (green lines) incident light for (a) the Vib 20V sample and an incidence angle of 70° and (b) the Alu 90V sample and an incidence angle of 15°.

The difference between the experimental and simulated spectra is quantified by computing the average over all wavelengths of the absolute relative difference between experimental and simulated data. This average absolute relative difference (in %) is defined as:

$$\frac{100}{N}\sum_{i=1}^{N}\frac{\left|R_{expe}(\lambda_i)-R_{simu}(\lambda_i)\right|}{\frac{1}{2}\times\left(R_{expe}(\lambda_i)+R_{simu}(\lambda_i)\right)}, \qquad (4)$$

where $R_{expe}(\lambda_i)$ and $R_{simu}(\lambda_i)$ are respectively the experimental and simulated reflectance spectra at a wavelength $\lambda_i$ and where $N$ is the total number of wavelengths of a spectrum, which is 431 in our case. The low $\Delta E_{94}$ value for the Vib 20V sample corresponds to a very good agreement between the simulated and experimental spectra for non-polarized light with an average relative difference of 2%. Very good agreement is also obtained for TM polarized light with an average relative difference of 1.6%, whereas a slightly higher difference is obtained for TE polarized light with a value of 4.1%. As expected from the $\Delta E_{94}$ value, the agreement between experimental and simulated spectra is worse for the Alu 90V sample, with average absolute relative differences of 22%, 23% and 21% respectively for non-polarized, TM and TE polarized incident light.

The global color prediction performance for all incidence angles can be evaluated by the average $\Delta E_{94}$ values presented in Fig. 8. To illustrate more visually the ability of our method to perform multi-angle color prediction, the chromatic path covered by the sample color when changing the incidence angle has been represented in a CIE 1931 xy chromaticity diagram [2] for the samples with the lowest (Vib 20V) and highest (Alu 90V) average $\Delta E_{94}$ (see Fig. 10). Whereas a very good color prediction is obtained for all angles for the Vib 20V sample, perceptible color differences are observed for the Alu 90V sample. For the latter, simulated colors are more saturated than experimental ones, with experimental colors chromaticity components closer to the D65 white point. Also, slight color hue differences are observed, corresponding to slight differences in the direction of the straight line passing through the D65 point and the experimental or simulated colors xy components.

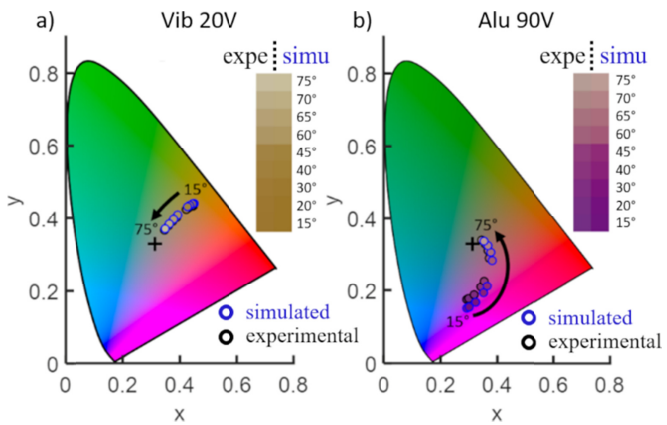

Fig. 10: Simulated and experimental chromatic paths in the CIE 1931 xy chromaticity diagram of (a) the Vib 20V and (b) the Alu 90V samples when changing the incidence angle. Is also represented on the right of each graph a comparison between the experimental (left) and simulated (right) colors of the samples for all 9 incidence angles. The black cross on each graph corresponds to the xy coordinates of the D65 white point.

To have a more quantitative analysis of the difference between simulated and experimental colors, the color components of the Vib 20V and Alu 90V samples have been converted into CIELCH color coordinates ( [27] and supplemental document). Then, for each color component, the relative variation (in %) between experimental and simulated data has been computed, through the following formula:

$$100 \times \frac{|X_{expe} - X_{simu}|}{\frac{1}{2} \times |X_{expe} + X_{simu}|} \qquad (5)$$

where $X_{expe}$ and $X_{simu}$ denote respectively the experimental and simulated color components.

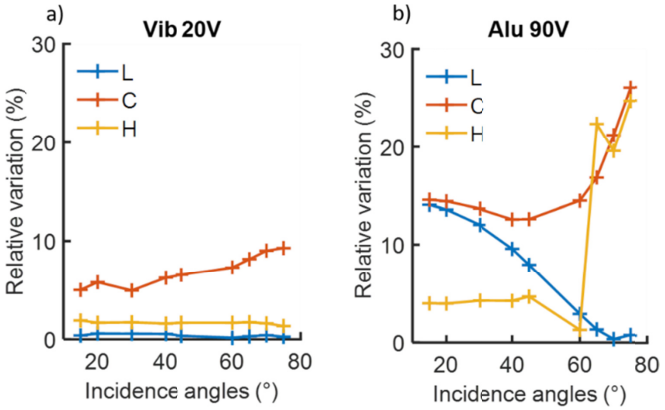


Fig. 11: Relative variation between experimental and simulated CIELCH color components for (a) the Vib 20V and (b) the Alu 90V samples as a function of the incidence angle.

The results are presented in Fig. 11. The good color prediction for the Vib 20V sample is related to very low relative variations (below 2% for all incidence angles) of the lightness L and hue H color components. Higher relative variations are nevertheless observed for the chroma C with values between 4% to 9%, meaning that the color chroma (or saturation) is the less well-predicted parameter. For the Alu 90V sample, all color components exhibit higher relative variations. The color hue is well predicted for incidence angles below 60° with relative variations below 5%, whereas the lightness has an opposite behavior with relative variations below 3% at incidence angles higher than 60°. As expected from the CIE 1931 xy chromaticity diagram, the color chroma is the less well-predicted component, with relative variations higher than 12% for all incidence angles. Note that due to the cyclic behavior of the hue, its absolute variations need also to be monitored: they are below 2° for the Vib 20V sample and below 10° for the Alu 90V sample.

Once studied the color prediction performances, the next section will be dedicated to the analysis of the material parameters obtained through the fit process.

### B. Material parameters

The values of the material parameters obtained after the fit process are presented in Fig. 12 for the five different sets of incidence angles $\{15°, 45°, 75°\}$, $\{20°, 40°, 70°\}$, $\{65°, 70°, 75°\}$, $\{15°, 20°, 30°\}$ and $\{15°, 30°, 45°, 60°, 75°\}$. These angle sets are the same as those presented in Fig. 7 to have all along the paper a complete characterization of the same angle sets. The values of the refractive index of layer number 2 (see Fig. 3) at 370 nm and 800 nm are represented instead of A, B and $X$ as different values for $A$, $B$ and $X$ can result in similar values of the refractive index. For example high $A$ and $B$ values and a high porosity $X$ can give a similar refractive index as low $A$ and $B$ values and a low porosity $X$. At first sight, it appears that the material parameters obtained with the fit on the angles set $\{15°, 20°, 30°\}$ are clearly different from the other ones for certain samples. It is particularly visible for $L_1$ (for all samples besides the Vib 10V sample), for $L_2$ (for the Alu 10V, Alu 90V and Vib 20V samples) and $L_3$ (for all samples besides Alu 10V and Alu 20V) as well as for the refractive index at both 370 nm and 800 nm wavelengths (for all samples besides Alu 90V and Vib 90V). A less pronounced discrepancy is also observed on certain samples for the $\{65°, 70°, 75°\}$ angles set, particularly for $L_1$ (for all samples besides Alu 10V and Vib 10V), for $L_2$ (for the Alu 20V and Alu 90V samples), for $L_3$ for the Alu 20V sample as well as for the refractive index at both wavelengths (for all samples besides Alu 10V, Vib 10V and Vib 90V). This discrepancy in the material parameter values is in agreement which what has been observed in Fig. 7 for the $\Delta E_{94}$ values, with generally worse $\Delta E_{94}$ for the $\{15°, 20°, 30°\}$ and $\{65°, 70°, 75°\}$ angle sets. Considering that these two angles sets don't give an acceptable color prediction, we will from now on focus on the material parameters given by the three remaining angle sets.

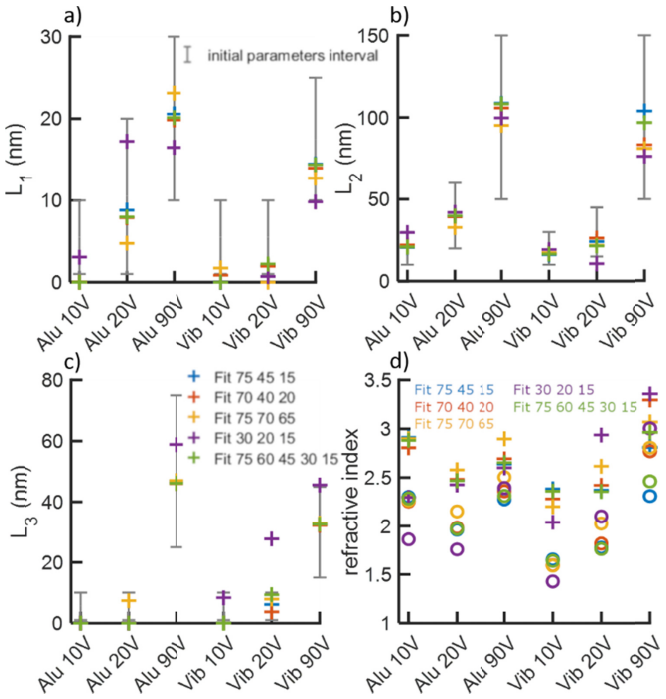


Fig. 12: Material parameters $L_1$ (a), $L_2$ (b) and $L_3$ (c) obtained after the fit process on the five different sets of incidence angles $\{15°, 45°, 75°\}$, $\{20°, 40°, 70°\}$, $\{65°, 70°, 75°\}$, $\{15°, 20°, 30°\}$ and $\{15°, 30°, 45°, 60°, 75°\}$. The error bars represent the initial parameters intervals of Table S2Table . (d) represents the refractive index of the layer number 2 (see Fig. 3) at wavelengths of 370 nm (+) and 800 nm (o) for the five different sets of incidence angles.

The angle sets $\{15°, 45°, 75°\}$, $\{20°, 40°, 70°\}$, and $\{15°, 30°, 45°, 60°, 75°\}$ don't give the same material parameters values. Their relative variations have been estimated by computing the following quantity:

$$\mathbf{100} \times \frac{\boldsymbol{\sigma}(\boldsymbol{P}_{\{15°,45°,75°\}}, \boldsymbol{P}_{\{20°,40°,70°\}}, \boldsymbol{P}_{\{15°,30°,45°,60°,75°\}})}{\boldsymbol{m}(\boldsymbol{P}_{\{15°,45°,75°\}}, \boldsymbol{P}_{\{20°,40°,70°\}}, \boldsymbol{P}_{\{15°,30°,45°,60°,75°\}})}, \quad \textbf{(6)}$$

with $P_x$ the material parameter value obtained from the angle set $x$, $\sigma(A_1, A_2, \dots A_n)$ the bias corrected standard deviation of the variables $A_1, A_2, \dots A_n$ and $m(A_1, A_2, \dots A_n)$ the average of the variables $A_1, A_2, \dots A_n$. The relative variations are presented in Fig. 13 for the thickness parameters $L_1, L_2$ and $L_3$ as well as for the refractive index of layer 2 at the wavelengths of 370 nm and 800 nm.

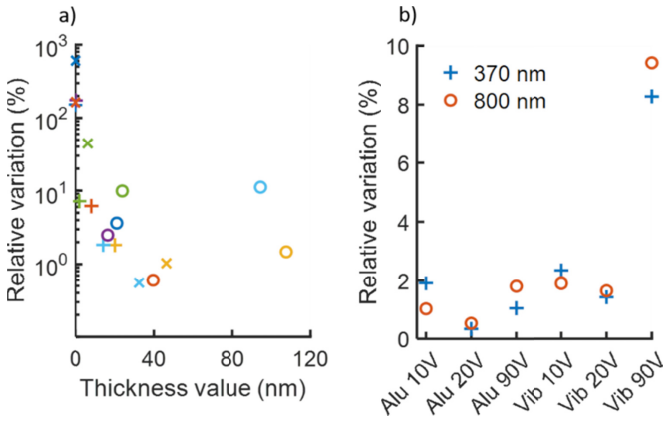


Fig. 13: Relative variation of (a) the material thickness parameters (+) $L_1$, (o) $L_2$ and (x) $L_3$ as a function of the parameter average value $m(P_{\{15°,45°,75°\}}, P_{\{20°,40°,70°\}}, P_{\{15°,30°,45°,60°,75°\}})$ and of (b) the refractive index of layer 2 at 370 nm and 800 nm, obtained from the angle sets $\{15°, 45°, 75°\}$, $\{20°, 40°, 70°\}$, and $\{15°, 30°, 45°, 60°, 75°\}$ for the 6 samples.

Very high relative variations are observed for the thickness parameters with for example a relative variation of about 600% for $L_3$ for the Alu 10V sample. Nevertheless, the very high relative variations are correlated to low values of the thickness parameter, with relative variations below 11% when the thickness value is higher than 10 nm. Also, high values of the relative variation are only observed for $L_1$ and $L_3$, which could be due to the fact that the composition of these layers has been set to a 50% - 50% mixture of the surrounding materials, which could highly differ from the real material composition are lead to a poor reliability of the determination of their thickness. The proposed method for the fit of the material thickness parameters has thus a relatively good reliability for thickness values higher than 10 nm. Considering the refractive index of layer 2, the relative variation is below 10% for all samples and both 370 nm and 800 nm wavelengths, and below 3% for all samples besides the Vib 90V sample. A relatively good reliability is thus obtained for determination of the refractive index of layer 2. Note that the relative variations presented in Fig. 13 are performed only on 3 different angle sets, which could reduce the variations. To check this, the same relative variations have been performed on the five angle sets giving the best results in terms of average and maximum $\Delta E_{94}$, which are$\{15°, 75°\}$, $\{45°, 75°\}$, $\{15°, 45°, 75°\}$, $\{20°, 40°, 70°\}$, and $\{15°, 30°, 45°, 60°, 75°\}$ (see Fig. 6). It corresponds to adding the angle sets $\{15°, 75°\}$ and $\{45°, 75°\}$ to the results of Fig. 13. The obtained results are very similar to these of Fig. 13, the main difference being observed for the Vib 10V sample for the relative variations of the refractive index. Relative variations of 6% and 9.5% are obtained for this sample, respectively at 370 nm and 800 nm.

To check the performance of the material parameters determination, the thicknesses have been compared to STEM images of FIB lamellae of the samples and the refractive index to refractive index values extracted from the literature, for titanium samples anodized in conditions close to the samples presented here. Only lamellae of the Vib 20V and Vib 90V samples have been prepared, which are the best suited samples for this technique, because the Vibromet series is the least rough series and the Vib 10V has a very thin oxide layer thickness ($L_1 + L_2 + L_3 = 16$ nm when determined with the angles set $\{15°, 45°, 75°\}$) which could

be difficult to measure with sufficient accuracy on the STEM images acquired in a FIB-SEM at 30 kV, on a heterogeneous layer. Table 1 presents the material parameters for all samples, in the case where the fit is done on the angles set $\{15°, 45°, 75°\}$. These data will be used for the thickness comparisons with the STEM images as well as for the refractive index comparison with literature data.

**Table 1. Values of the material parameters obtained after the fit process for all samples. The fit is done on the three incidence angles 15°, 45° and 75°.**

| Sample name | $A$ | $B$ ($\mu m^{-2}$) | $L_3$ (nm) | $L_2$ (nm) | $L_1$ (nm) | $X$ |
|---|---|---|---|---|---|---|
| Alu 10V | 3.22 | 0.21 | 0 | 21 | 0 | 0.46 |
| Alu 20V | 2.05 | 0.11 | 0 | 40 | 9 | 0.21 |
| Alu 90V | 2.91 | 0.10 | 47 | 109 | 21 | 0.37 |
| Vib 10V | 1.51 | 0.14 | 0 | 16 | 0 | 0.10 |
| Vib 20V | 2.29 | 0.22 | 6 | 24 | 2 | 0.49 |
| Vib 90V | 3.05 | 0.15 | 32 | 104 | 14 | 0.41 |

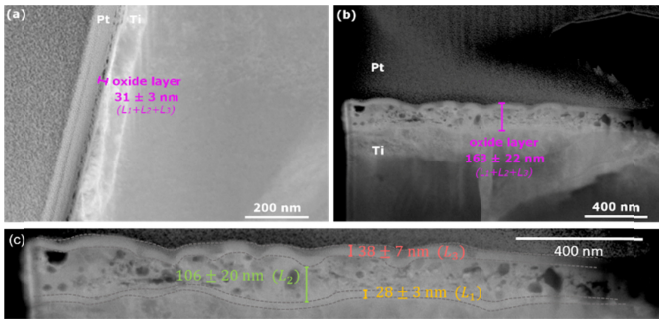


Fig. 14. STEM images of FIB lamellas cut out from the samples anodized at maximum cell potentials of (a) 20 V and (b)-(c) 90 V from the Vibromet series. (c) is a zoom of figure (b) where the 3 sublayers of the oxide layer have been highlighted. All oxide thicknesses have been measured on 20 different positions on the images. The averages and the standard deviations over these measurements are shown on each figure. Adapted with permission (Elsevier) from [28].

STEM images of FIB lamellae of the Vib 20V and Vib 90V samples are presented on Fig. 14. Both oxide layers seem to present porosities, here shown as dark areas inside the oxide layer in these dark field images. Fig. 14 (c) is a zoom of Fig. 14 (b) where it can be observed that the oxide layer of the Vib 90 V sample seems to be split in three sublayers, with a porous middle layer, and two more homogeneous external sublayers. A similar structure is hardly visible in Fig. 14 (a) for the Vib 20V sample, mainly because of the thin oxide thickness of this sample which is close to the resolution limit of the STEM image.

Note that such an oxide layer structure with 3 sublayers has been already observed in the literature on anodized titanium samples [21]. 20 measurements of the total oxide layer and sublayer thicknesses have been performed on different positions on the images. Fig. 14 shows the averages and the standard deviations over these measurements. The oxide thickness measurement uncertainty is thus due to the uncertainty in determining the top and bottom edges of the layer on the image, as well as to oxide thickness variations inside the observed area. The oxide thickness variations are clearly visible for the 90 V sample.

A total oxide thickness of 31 ± 3 nm has been measured on the Vib 20 V sample, which is in agreement with the sum $L_1 + L_2 + L_3 = 32$ nm obtained from the material parameter fit on the reflectance spectra (see Table 1). For the Vib 90 V sample, a total oxide thickness of 163 ± 22 nm has been measured, which is again in agreement with the sum $L_1 + L_2 + L_3 = 151$ nm extracted from Table 1. Moreover, for the Vib 90 V sample, the sublayer thicknesses extracted from the STEM images are also in relatively good agreement with the $L_1, L_2$ and $L_3$ values of Table 1, with respectively 28 ± 3 nm and 14 nm for $L_1$, 106 ± 20 nm and 104 nm for $L_2$, 38 ± 7 nm and 32 nm for $L_3$. The oxide thickness standard deviations obtained from the STEM images are in the range 10% to 20% of the average value, which is coherent with the relative variations of the material thickness parameters obtained with the fit process (see Fig. 13 (a)), which reach a maximum value of about 11%. Note that we consider here for the Vib 20V sample the relative variation on the sum $L_1 + L_2 + L_3$ which is equal to 11% and given by:

$$100 \times \frac{\sqrt{\sigma(L_1)^2 + \sigma(L_2)^2 + \sigma(L_3)^2}}{m(L_1) + m(L_2) + m(L_3)}, \qquad (7)$$

where $\sigma(L_i)$ and $m(L_i)$ designates respectively the bias corrected standard deviation and the average value of the thickness of layer $i$ over the values obtained from the angle sets $\{15°, 45°, 75°\}$, $\{20°, 40°, 70°\}$, and $\{15°, 30°, 45°, 60°, 75°\}$ (cf. equation (6)).

The material thickness parameters obtained from the fit process of the reflectance spectra correspond to average thickness values over the illuminated area of the sample, which is 10 x 2 mm at normal incidence and 10 x 7.7 mm at an incidence angle of 75°. The uncertainties on these average values are thus likely to be lower than the variations observed on the STEM images, which are measured on a length of about 0.7 µm for the Vib 20V sample and 2 µm for the Vib 90V sample.

Fig. 15 presents the refractive index values of the layer 2 (taking into account its porosity) as a function of the wavelength, corresponding to the $A, B$ and $X$ values of Table 1, for all the samples. These refractive index values have been compared to different references: Joseph et al. [29], the two different results presented by Van Gils et al. in [16] for samples anodized at 10 V and 80 V, the two different results presented by Blondeau et al. in [30] (for the case of titanium samples anodized in 0.5M $H_2SO_4$) and attributed to amorphous and anatase $TiO_2$ and the two different results presented by Diamanti et al. in [31] for samples anodized at 60 V and 90 V. Note that all of these references correspond to anodized titanium samples prepared in conditions close to ours, with an electrolyte composed of 0.5M $H_2SO_4$ for [16,30,31] and 1M $H_2SO_4$ for [29], and an anodizing voltage in the range [1 V- 100 V], despite some differences in the current density values. Also, these references compute the global refractive index of the oxide layer depending on both the $TiO_2$ phase and the layer potential porosity.

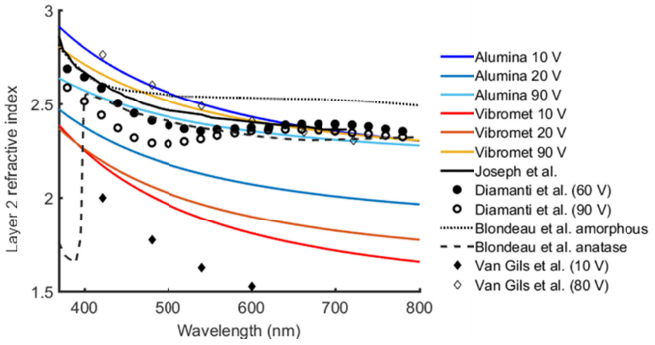


Fig. 15. Refractive index of the layer 2 (taking into account its porosity) as a function of the wavelength, corresponding to the $A$, $B$ and $X$ values of Table 1, for all the samples. These refractive index values have been compared to different references: Joseph et al. [29], the two different results presented by Van Gils et al. in [16] for samples anodized at 10 V and 80 V, the two different results presented by Blondeau et al. in [30] (for the case of titanium samples anodized in 0.5M $H_2SO_4$) and attributed to amorphous and anatase $TiO_2$ and the two different results presented by Diamanti et al. in [31] for samples anodized at 60 V and 90 V.

Alu 10 V, 90 V and Vib 90 V samples exhibit refractive index values for their layer 2 comparable to references [29–31] and the 80 V sample of reference [16]. Alu 20 V and particularly Vib 10 V and Vib 20 V samples exhibit lower refractive index values. Van Gils et al. also observe very low refractive index values for their 10 V sample. They relate these low values to the formation of a microporous structure due to gas evolution during the anodizing process for a low anodizing voltage.

The layer 2 refractive index values obtained from the fit of the reflectance spectra with the angles set $\{15°, 45°, 75°\}$ are thus coherent with the oxide layer refractive index values found in the literature for similar samples. Nevertheless, more advanced studies of the oxide layer porosity, chemical composition, crystallinity would be necessary to confirm whether the variations of the layer 2 refractive index correspond to phase changes of the oxide or porosity changes of the layer.

## 4. Conclusion

The present study deals with the prediction of the whole chromatic path travelled by the colors of glossy anodized titanium samples in every specular geometry. The study is based on measurements of the samples reflectance spectra for TE and TM polarized incident light in a limited number of specular geometries. It allows to obtain the oxide layer structural parameters (thickness, refractive index) which are then put into a three layers Abeles matrices based optical model to predict the samples reflectance spectra in every specular geometry. Fitting the material parameters on incidence angle sets composed of either 2 or 3 angles gives results comparable to those obtained with a 5-angles angle set, as long as the 2 or 3 angles are properly chosen. The best color prediction performances are obtained with the angle sets $\{45°, 75°\}$ and $\{15°, 45°, 75°\}$. These angle sets give average and maximum $\Delta E_{94}$ color distance values between predicted and measured colors (computed over 9 different incidence angles and for the 6 samples considered in the study) respectively of about 1.9 and 5. The oxide layer structural parameters obtained through the fit process are compared with either values extracted from the literature (for the refractive index) or STEM images of FIB lamellae of certain samples (for the layer thicknesses): a good agreement is obtained for all parameters. Simpler two-layer models will also be tested in the future to compare their performances with the present three-layer model.

Note that the present study doesn't permit to predict the sample colors in non-specular conditions. A further extension is in progress, based on the model proposed by Roos et al. [32], which is able to predict the diffuse reflectance of oxidized metals from the specular Fresnel coefficients of the interfaces as well as the interfaces Root Mean Square roughness.

**Funding.**

**Acknowledgments.** This work was supported by the LABEX MANUTECH-SISE (ANR-10-LABX-0075) of Université de Lyon, within the program "Investissements d'Avenir" (ANR-11-IDEX-0007) operated by the French National Research Agency (ANR). The collaboration between Mines Saint-Etienne and Politecnico di Milano on this study was partly funded by the CMIRA program for international collaborations of Region Auvergne Rhone-Alpes.

**Disclosures.** The authors declare no conflicts of interest.

**Data availability.** Data underlying the results presented in this paper are not publicly available at this time but may be obtained from the authors upon reasonable request.

**Supplemental document**. See Supplement 1 for supporting content.

## References

1. M. E. Nadal and E. A. Early, "Color Measurements for Pearlescent Coatings," Color Res. Appl. **29**, 38–42 (2004).
2. S. K. Shevell, ed., *The Science of Color*, 2nd ed. (Elsevier, 2003).
3. F. J. J. Clarke, R. McDonald, and B. Rigg, "Modification to the JPC79 Colour–difference Formula," J. Soc. Dye. Colour. **100**, 128–132 (1984).
4. A. Ferrero, A. Rabal, J. Campos, F. Martínez-Verdú, E. Chorro, E. Perales, A. Pons, and M. L. Hernanz, "Spectral BRDF-based determination of proper measurement geometries to characterize color shift of special effect coatings.," J. Opt. Soc. Am. A. Opt. Image Sci. Vis. **30**, 206–14 (2013).
5. A. Ferrero, J. Campos, E. Perales, F. M. Martínez-Verdú, I. van der Lans, and E. Kirchner, "Global color estimation of special-effect coatings from measurements by commercially available portable multiangle spectrophotometers," J. Opt. Soc. Am. A **32**, 1 (2015).
6. E. Højlund-Nielsen, J. Weirich, J. Nørregaard, J. Garnaes, N. Asger Mortensen, and A. Kristensen, "Angle-independent structural colors of silicon," J. Nanophotonics **8**, 083988 (2014).
7. J. Kim, S. H. Jhi, and K. Ryeol Lee, "Color of TiN and ZrN from first-principles calculations," J. Appl. Phys. **110**, (2011).
8. J. Baxter, A. Calà Lesina, J. M. Guay, A. Weck, P. Berini, and L. Ramunno, "Plasmonic colours predicted by deep learning," Sci. Rep. **9**, 1–9 (2019).
9. Q. Cridling, R. Charriere, D. Jamon, M. V. Diamanti, M. P. Pedeferri, and D. Delafosse, "Study of the influence of roughness on the gonioapparency of anodized titanium," in *IS and T International Symposium on Electronic Imaging Science and Technology* (2017), Vol. Part F1300.
10. M. V Diamanti, B. Del Curto, M. Ormellese, and M. P. Pedeferri, "Photoactive and colored anodic oxides on titanium for architectural and design applications," Tech. Proc. 2008 Clean Technol. Conf. Trade Show **1**, 170–173 (2008).
11. T. Wang, L. Wang, Q. Lu, and Z. Fan, "Changes in the esthetic, physical, and biological properties of a titanium alloy abutment treated by anodic oxidation," J. Prosthet. Dent. **121**, 156–165

(2018).
12. M. V Diamanti, B. Del Curto, M. P. Pedeferri, and P. Milano, *Colored Titanium Oxides : From Jewelry to Biomedical Applications* (Elsevier, 2018).
13. A. Karambakhsh, A. Afshar, S. Ghahramani, and P. Malekinejad, "Pure Commercial Titanium Color Anodizing and Corrosion Resistance," J. Mater. Eng. Perform. **20**, 1690–1696 (2011).
14. M. Manjaiah and R. F. Laubscher, "Effect of anodizing on surface integrity of Grade 4 titanium for biomedical applications," Surf. Coatings Technol. **310**, 263–272 (2017).
15. U. Balaji and S. K. Pradhan, "Titanium anodisation designed for surface colouration - Systemisation of parametric interaction using response surface methodology," Mater. Des. **139**, 409–418 (2018).
16. S. Van Gils, P. Mast, E. Stijns, and H. Terryn, "Colour properties of barrier anodic oxide films on aluminium and titanium studied with total reflectance and spectroscopic ellipsometry," Surf. Coatings Technol. **185**, 303–310 (2004).
17. I. Komatsu, H. Aoki, M. Ebisawa, A. Kuroda, K. Kuroda, and S. Maeda, "Color change mechanism of niobium oxide thin film with incidental light angle and applied voltage," Thin Solid Films **603**, 180–186 (2016).
18. C. V Manzano, J. J. Schwiedrzik, G. Bürki, J. Michler, and L. Philippe, "Deterministic Model of Observed Colours on Metal-Anodic Aluminium Oxide-Al Nanostructures," 0–13 (2020).
19. F. Abelès, "La theorie generale des couches minces," Le J. Phys. le Radium **11**, 307–309 (1950).
20. D. Whitehouse, *Surfaces and Their Measurement* (Elsevier, 2002).
21. L. Bartlett, "Variability in coloured titanium surfaces for jewellery," PhD Thesis, University of the Arts London (2009).
22. H. Fujiwara, *Spectroscopic Ellipsometry* (Wiley, 2007).
23. D. W. Lynch, C. G. Olson, and J. H. Weaver, "Optical properties of Ti, Zr, and Hf from 0.15 to 30 ev," Phys. Rev. B **11**, 3617 (1975).
24. M. V. Diamanti and M. P. Pedeferri, "Effect of anodic oxidation parameters on the titanium oxides formation," Corros. Sci. **49**, 939–948 (2007).
25. D. A. G. Bruggeman, "Berechnung verschiedener physikalischer Konstanten von heterogenen Substanzen," Ann. Phys. **24**, 636 (1935).
26. *Commission Internationale de l'éclairage, Norme 61966-2-1* (1999).
27. J. Schanda, ed., *Colorimetry: Understanding the CIE System* (Wiley, 2007).
28. Q. Cridling, R. Charriere, D. Jamon, M. Lenci, M. P. Pedeferri, and D. Delafosse, "Anodized titanium oxide thickness estimation with ellipsometry, reflectance spectra extrema positions and electronic imaging: importance of the interfaces electromagnetic phase-shift," Thin Solid Films **709**, 138181 (2020).
29. J. Joseph and A. Gagnaire, "Ellipsometric study of anodic oxide growth: Application to the titanium oxide systems," Thin Solid Films **103**, 257–265 (1983).
30. G. Blondeau, M. Froelicher, M. Froment, and A. Hugot-Le Goff, "On the optical indices of oxide films as a function of their crystallization: Application to anodic TiO2(anatase)," Thin Solid Films **42**, 147–153 (1977).
31. M. V. Diamanti, B. Del Curto, and M. Pedeferri, "Interference colors of thin oxide layers on titanium," Color Res. Appl. **33**, 221–228 (2008).
32. A. Roos, M. Bergkvist, and C. Ribbing, "Optical scattering from oxidized metals. 1: Model formulation and properties," Appl. Opt. **28**, 1360 (1989).